

Limiting Phase Separation via Halogen-free Solvent Slot-die Processing Enables Highly Efficient and Eco-Friendly All-Polymer Solar Cells

Baohua Wu, ‡^a Yuxin Kong, ‡^b Qinglian Zhu, ^a Sen Zhang, ^a Baojun Lin, ^a Heng Zhao, ^a
Jingwei Xue, ^a Susanne Seibt, ^c Ke Zhou, ^{*a} Yuxiang Li, ^{*b} and Wei Ma ^{*a}

Supporting Information

Experiment section

Materials. The polymer PBDB-T and PZT- γ were synthesized according to procedures reported in the literature^[1]. The patterned glass/ITO substrates were purchased from South China Science & Technology Co., Ltd.

Electrochemical characterizations. Cyclic voltammetry was carried out on a AUTOLAB PGSTAT302N electrochemical workstation with three electrodes configuration, using Ag/AgCl as the reference electrode, a Pt plate as the counter electrode, and a glassy carbon as the working electrode. 0.1 mol L⁻¹ tetrabutylammonium hexafluorophosphate in anhydrous acetonitrile was used as the supporting electrolyte. Polymers were drop-cast onto the glassy carbon electrode from chloroform solutions (10 mg/mL) to form thin films. Potentials were referenced to the ferrocenium/ferrocene couple by using ferrocene as external standards in acetonitrile solutions. The scan rate is 100 mV s⁻¹.

Device Fabrication. The BHJ devices were fabricated with an inverted device structure of Glass/ITO/ZnO/active layer/MoO_x/Al. The patterned ITO substrate was continuously cleaned three times by sonication in water with detergent, deionized water, acetone, and isopropanol for 30 min of each step. Then the substrate was dried with a nitrogen gun. After ultraviolet ozone treatment for 20 min, the ZnO precursor was spin-coated on the ITO substrate at 4500 rpm to form an electron transporting layer ZnO. Then, the substrate was baked at 200 °C for 30 min. The active layer solution was prepared in chlorobenzene and o-xylene at a total concentration of 14 mg/mL ($P_D/P_A = 1:1$ by weight) without any additives. After that, a 100 nm film of the active layer was coated by slot-die coating in ambient conditions. For the slot-die coating, the solution was pumped onto a moving substrate through the slot in the coating head. The gap between the substrate and the head was 100 μm. The slot-die head and substrate temperature were controlled by heating element. The optimal speed of the substrate and the injection speed of the solution were adjusted according to different combination of solution temperature and substrate temperature. The final BHJ films were transferred to the N₂-filled glovebox without any further treatment. Finally, a 10 nm MoO_x and 100 nm Al were sequentially deposited as anode below the vacuum level of 1×10^{-4} Pa. The effective area of one cell is 4 mm².

Characterization. The temperature-dependent UV–vis absorption spectra and film UV–vis absorption spectrum was measured by a Shimadzu UV-3600 Plus Spectrophotometer. The film thickness was measured by a surface profilometer (Dektak XT, Bruker). The J – V characteristics were performed in a N₂-filled glovebox under AM 1.5G (100 mW/cm²) using a Keithley 2400 source meter unit and an AAA solar simulator

(SS-F5-3A, Enli Technology CO., Ltd.) calibrated by a standard Si photovoltaic cell with a KG5 filter. The EQE was measured by a solar cell spectral response measurement system (QE-R3018, Enli Technology CO., Ltd.) with the calibrated light intensity by a standard single-crystal Si photovoltaic cell. AFM characterization was scanned by Veeco INNOVA Atomic Force Microscope using a tapping mode. PL spectrum was recorded by FLS1000 spectrometer (Edinburgh Instruments, EI).

Pseudo Free-standing Tensile Test. The samples were prepared through following steps. First, active layers were slot-die coated on 1 cm×3 cm glasses covered with water soluble PEDOT:PSS layer (≈ 60 nm) to form a bilayer composite film structure with a semiconducting film of 100 nm thick. Then, the films were etched into the dog-bone shape through an oxygen plasma etcher with a dog-bone shaped PDMS mask for 10 min. The bilayer film was slowly dipped into a deionized water bath to release and float the dog-bone photovoltaic films by dissolving the underlying water-soluble PEDOT:PSS layer. Tensile grips were slowly descended to adhere with films on water. The tensile test was performed by applying strains at 9×10^{-2} %/s to the film through a motorized linear stage equipped with a digital encoder while monitoring the force exerted on the film with a high-resolution load cell.

Hole and Electron Mobility Measurements. The mobilities were measured by using a space charge limited current (SCLC) model with the hole-only device of glass/ITO/PEDOT:PSS/active layer/MoO_x/Al and electron-only device of glass/ITO/ZnO/active layer/PDINO/Al. Hole mobility and electron mobility were obtained by fitting the current density-voltage curves and calculated by the equation^[2]:

$$J = 9\epsilon_0\epsilon_r\mu(V_{appl} - V_{bi} - V_s)^2/8L^3$$

Where J is current density, ϵ_0 is the permittivity of free space, ϵ_r is the relative permittivity of the material (assumed to 3), μ is hole mobility or electron mobility, V_{appl} is applied voltage, V_{bi} is the built-in voltage due to the relative work function difference of the two electrodes, V_s is the voltage drop from the substrate's series resistance ($V_s=IR$) and L is the thickness of active layer.

Grazing Incidence Wide-Angle X-ray Scattering (GIWAXS) Characterization.

GIWAXS measurements were performed at SAXS/WAXS beamline, Australian Synchrotron ANSTO. Samples were prepared on Si substrates using identical blend solutions as those used in devices. The 15.2 keV X-ray beam was incident at a grazing angle of 0.08° - 0.12° , selected to maximize the scattering intensity from the samples. The scattered x-rays were detected using a Dectris Pilatus 2M photon counting detector.

Resonant Soft X-ray Scattering (RSoXS).

R-SoXS^[3,4] transmission measurements were performed at beamline 11.0.1.2 at the Advanced Light Source. Samples for R-SoXS measurements were prepared on a PSS modified Si substrate under the same conditions as those used for device fabrication, and then transferred by floating in water to a 1.5 mm \times 1.5 mm, 100 nm thick Si₃N₄ membrane supported by a 5 mm \times 5 mm, 200 μ m thick Si frame (Norcada Inc.). 2D scattering patterns were collected on an in-vacuum CCD camera (Princeton Instrument PI-MTE). The sample detector distance was calibrated from diffraction peaks of a triblock copolymer poly(isoprene-*b*-styrene-*b*-2-vinyl pyridine), which has a known spacing of 391 Å. The beam size at the sample is approximately 100 μ m by 200 μ m. Near the carbon absorption edge (around 285 eV, which is in the soft X-ray range), the index of refraction of polymers varies drastically and uniquely, yielding extremely varying and high contrast^[5]. In our

systems, the index of refraction of materials also varies drastically and uniquely near the carbon absorption edge. We have employed the R-SoXS measurements at different energy (270, 282, 283, 284.2, 284.8, 285.2, 285.8, 286.8 eV) near the carbon absorption edge to get the high contrast. Finally, we found the scattering at 284.2 eV get the highest contrast. The relative domain purity can be extracted by integrating the R-SoXS scattering profiles via total scattering intensity (TSI). (Modern Aspects of Small-Angle Scattering. Kluwer Academic Publishers: Dordrecht, 1995, 45, 463. Colloid Polym. Sci. 1952, 125, 108. Small Angle X-ray Scattering (Eds: O. Glatter, O. Kratky), Academic Press, London 1982.)

$$TSI = \int_0^{\infty} I(q)q^2dq = 2\pi^2V \sum_{i \neq j} \Delta\rho_{ij}^2 \phi_i \phi_j$$

where $\Delta\rho_{ij}$ is for the conventional SAXS the difference in electron density between the i^{th} and j^{th} phases, ϕ_i is the volume fraction of i^{th} phase and it follows that $\sum \phi_i = 1$. Note that $\Delta\rho_{ij}$ becomes the difference in composition between the i^{th} and j^{th} phases in R-SoXS and $\Delta\rho_{ij}^2$ is proportional to the optical contrast of $\Delta n^2 = \Delta\delta_{ij}^2 + \Delta\beta_{ij}^2$, where $\Delta\delta_{ij}$ and $\Delta\beta_{ij}$ are the difference of dispersive and absorptive optical constants, respectively. Subsequently it is helpful to define Δc_{ij} as a parameter describing the average composition variation between the i^{th} and j^{th} phases. The TSI expression can then be rewritten as

$$TSI = \int_0^{\infty} I(q)q^2dq = 2\pi^2V \sum_{i \neq j} \Delta c_{ij}^2$$

To be more specific, in a two-phase system the TSI can be simplified to

$$TSI = \int_0^{\infty} I(q)q^2 dq = 2\pi^2 V \Delta \rho_{12}^2 \phi_1 \phi_2 = 2\pi^2 V \Delta c_{12}^2$$

where $\phi_2 = 1 - \phi_1$. Given the straightforward relation between ϕ_1 and ϕ_2 , the average composition variation is proportional to domain purity^[6].

In-situ Ultraviolet-visible (UV-vis) Absorption Measurements.

In-situ UV-vis absorption measurements were performed by the Filmetrics F20-EXR spectrometer using the transmission mode with the time resolution of 0.02 s. The spectrometer consists of light source and detector. The light source and detector are fixed above and below the substrate, respectively, and on the same vertical line. The solution was injected into the slot and the film was coated onto the glass substrate. The detector collects the transmission spectra ranged from 400 to 1050 nm during coating. The UV-vis absorption spectra are calculated from the transmission spectra according to the equation $A_\lambda = -\log_{10}(T)$, where A_λ is the absorbance at a certain wavelength (λ) and T is the calculated transmittance. The light source and detector were turned on before coating the film, so time zero is the point when the first solution transmission spectrum was collected by the detector. Before time zero, there is only noise in the transmission spectra.

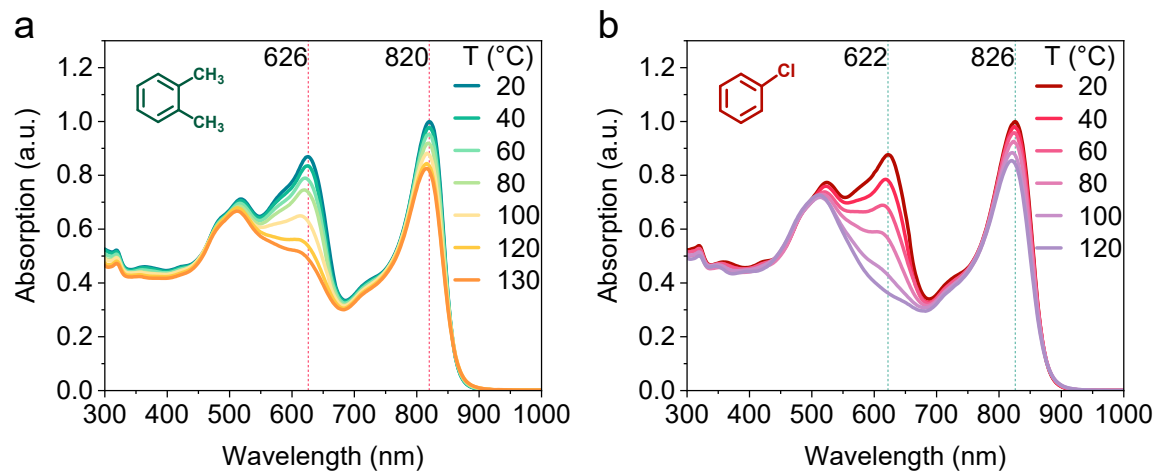


Fig. S1 Temperature-dependent UV-vis absorption spectra of PBDB-T:PZT- γ blend solution in (a) o-XY and (b) CB.

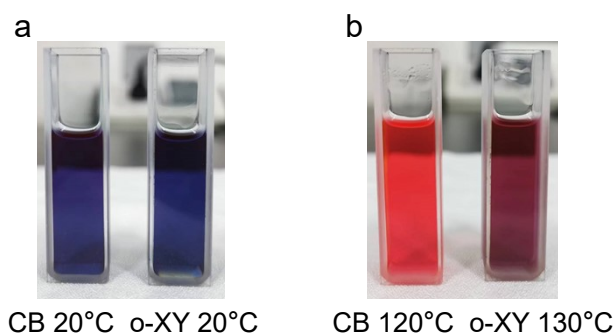


Fig. S2 PBDB-T dissolves in CB and o-XY at different temperatures (Solution concentration is 0.03 mg/ml).

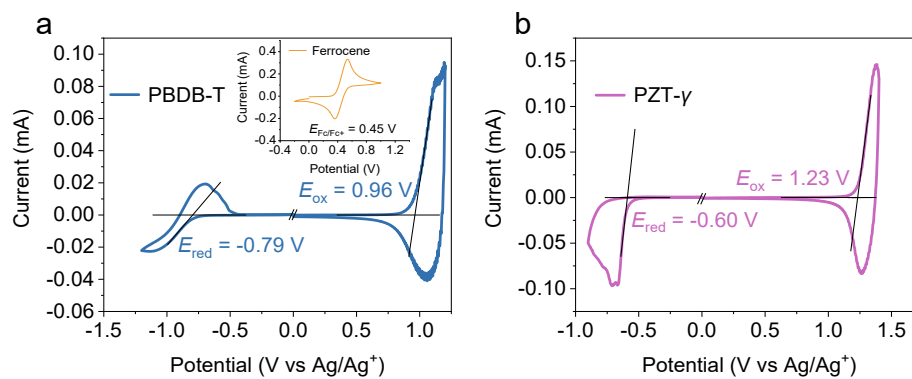


Fig. S3 Cyclic voltammetry curves of PBDB-T and PZT- γ .

Table S1 Photovoltaic parameters of all-PSCs based on PBDB-T:PZT- γ blend under different processing conditions.

Solvent	Solution Tem. [°C]	V_{oc} [V]	J_{sc} [mA/cm ²]	FF [%]	PCE [%]
o-XY	20	0.891	17.54	43.13	6.74
	50	0.902	21.81	46.69	9.19
	110	0.871	23.96	64.65	13.49
	120	0.874	24.08	67.44	14.19
	130	0.874	24.68	69.56	15.01
	140	0.872	24.52	68.60	14.67
CB	50	0.919	22.98	53.33	11.26
	90	0.896	23.77	56.69	12.07
	100	0.894	24.71	60.09	13.27
	110	0.890	24.29	59.47	12.86

Table S2 Comparison of our results with reported all-PSCs processed with green solvent^[7].

Processing methods	All-Polymer Systems	Solvent	V_{oc} [V]	J_{sc} [mA/cm ²]	FF [%]	PCE [%]	Ref.
Spin coating	P2F-Si:PNDICl	d-Limonene	0.99	6.6	64.0	4.2	[8]
	PTzBI-Si:PNDICl	CPME	0.81	10.6	63.5	5.4	[8]
	PiI-2T-PS10:P(TP)	Toluene:CN	0.98	10.1	51	5.1	[9]
	PTB7-Th:PNDI2OD-T2	o-XY:DMAc	0.79	14.8	52	6.08	[10]
	J51:N2200	Mes	0.80	12.23	64.22	6.28	[11]
	PBDT-TS1:PPDIODT	Anisole	0.76	15.7	55.1	6.58	[12]
	J51:N2200	CPME	0.82	14.2	60.2	7.6	[13]
	J51:PTB7-Th:N2200	CPME	0.82	17.3	67.8	9.6	[13]
	PTzBI-Si:N2200	2-MeTHF:DBE	0.86	15.8	73.1	10.1	[14]
	PTzBI-Si:N2200	CPME:DBE	0.85	16.5	77.9	11.0	[14]
	PBTA-Si:PTzBI-Si:N2200	2-MeTHF:DBE	0.82	17.5	72.1	10.4	[15]
	PM6:PZ1	Toluene:CN	0.96	17.1	68.2	11.2	[16]
	PTzBI-Si ₁₁ :N2200	CPME:DBE	0.85	17.2	77.9	11.5	[17]
	Nap-SiBTz:N2200	Toluene:1-PN	0.84	19.2	70.08	11.7	[18]
	PM6:PTer-N25	o-XY:2-MN	0.94	19.52	65.13	11.94	[19]
	PTzBI-oF:PS1	2-MeTHF:DBE	0.918	22.47	66.70	13.74	[20]
	PM6:PY2F-T	o-XY:CN	0.86	22.64	71.87	14.03	[21]
	PBDB-T:PJ1	o-XY:DMN	0.90	21.92	72.61	14.34	[22]
	PBDB-T:PJ1:PJ2	o-XY:DMN	0.91	21.46	72.98	14.28	[22]
	PM6:PY-IT	Toluene:CN	0.933	22.52	73.8	15.51	[23]
PM6:L14	o-XY:1-MN	0.953	22.1	74.1	15.6	[24]	
PBQ6:PYF-T- <i>o</i>	Toluene:DTT	0.886	25.12	76.64	17.06	[25]	
Blade coating	PBDT-TS1:PPDIODT	o-MA	0.74	12.8	53.4	5.21	[26]
	PBDT-TS1:PPDIODT	o-MA:DPE	0.74	13.77	52.46	5.6	[27]
	PTzBI:N2200	MeTHF	0.84	14.86	66.65	8.36	[28]
Slot-die coating	PTzBI-Si:N2200	2-MeTHF	0.88	17.6	75.8	11.8	[29]
	PBDB-T:PZT- γ	o-XY	0.874	24.68	69.56	15.01	This Work

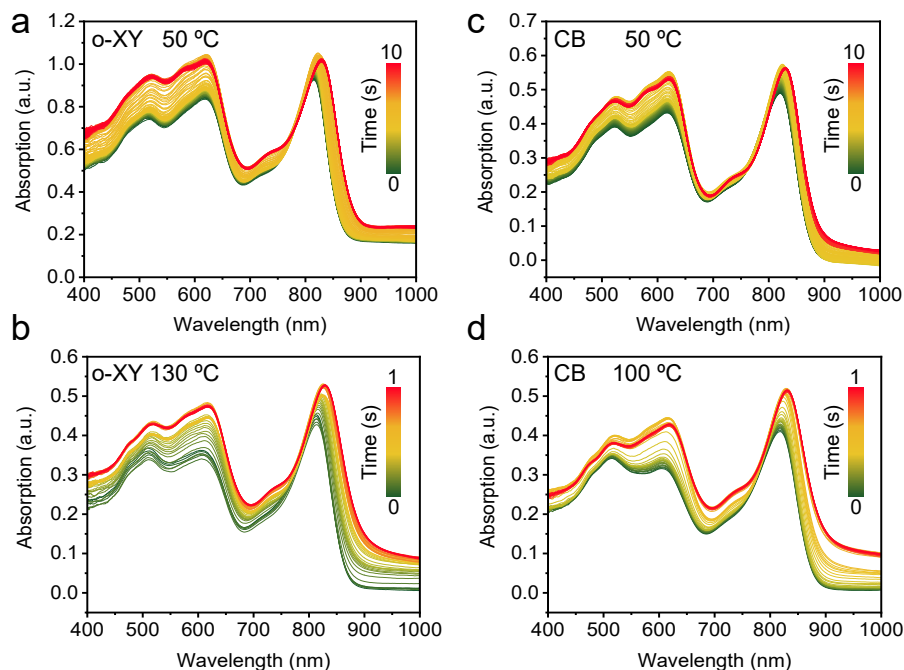


Fig. S4 In-situ UV-vis absorption spectra of PBDB-T:PZT- γ blend films during slot-die coating.

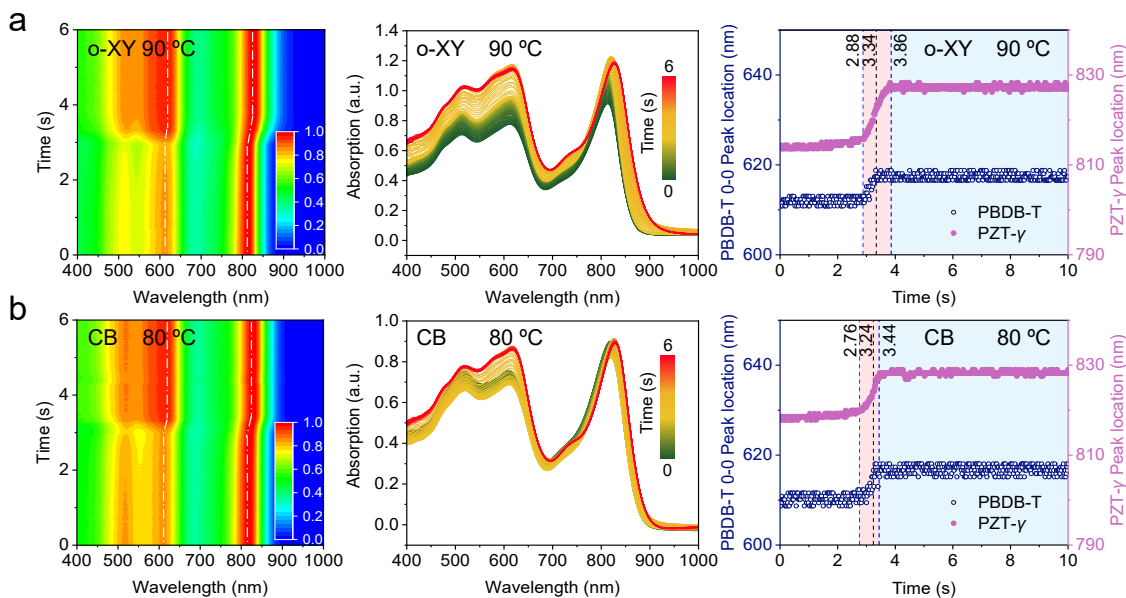


Fig. S5 Time evolution of normalized UV-vis absorption spectra, in-situ UV-vis absorption spectra and the peak position evolution of PBDB-T and PZT- γ during slot-die coating with o-XY at 90 °C (a) and with CB at 80 °C (b).

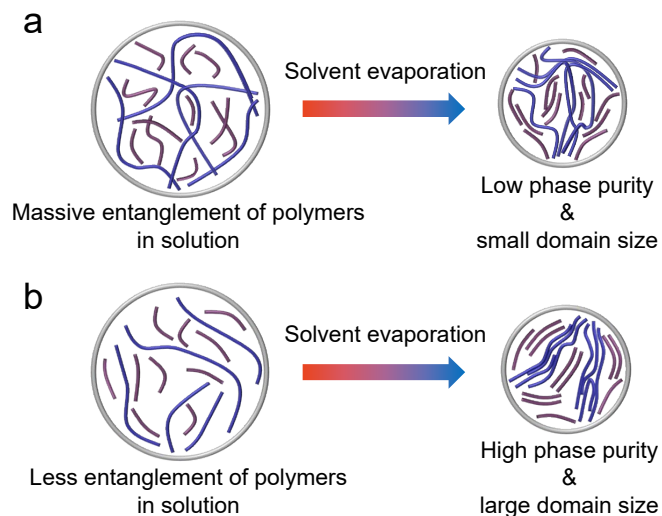


Fig. S6 Schematic illustration of phase separation process when solutions with different entanglement degrees of polymers are transformed into films.

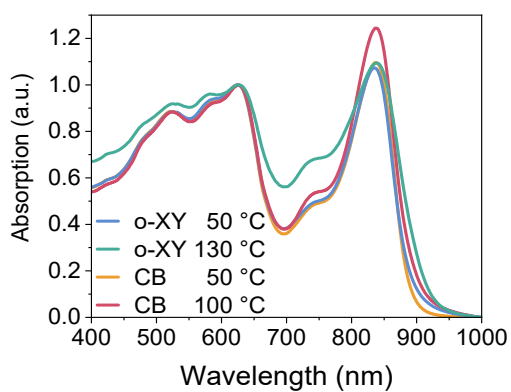


Fig. S7 Normalized ultraviolet-visible (UV-vis) absorption spectra of PBDB-T:PZT- γ films with different processing conditions.

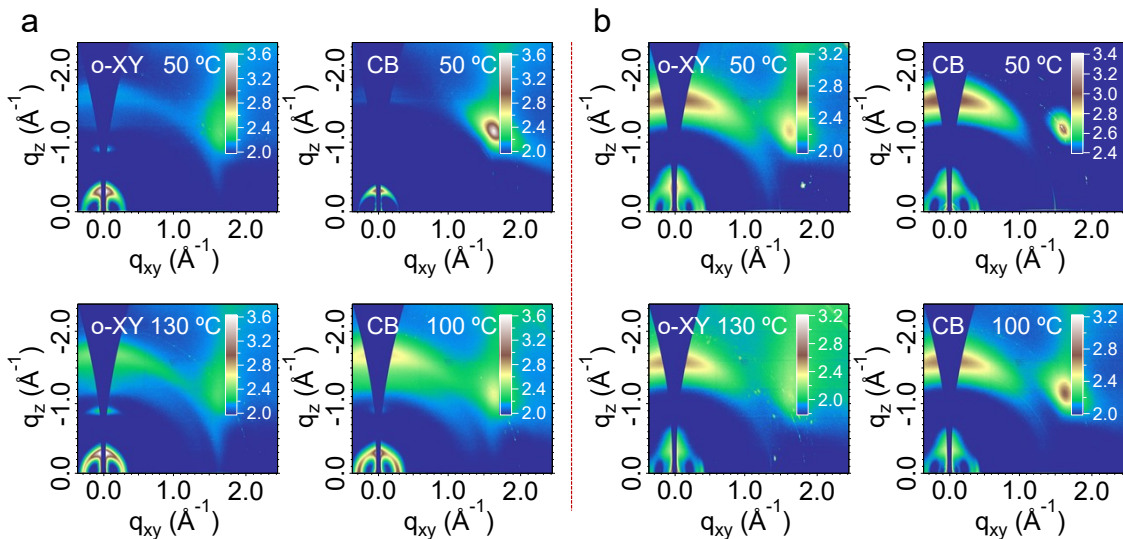


Fig. S8 2D-GIWAXS images of neat PBDB-T (a) and PZT- γ (b) films processed with different solvents at different temperatures.

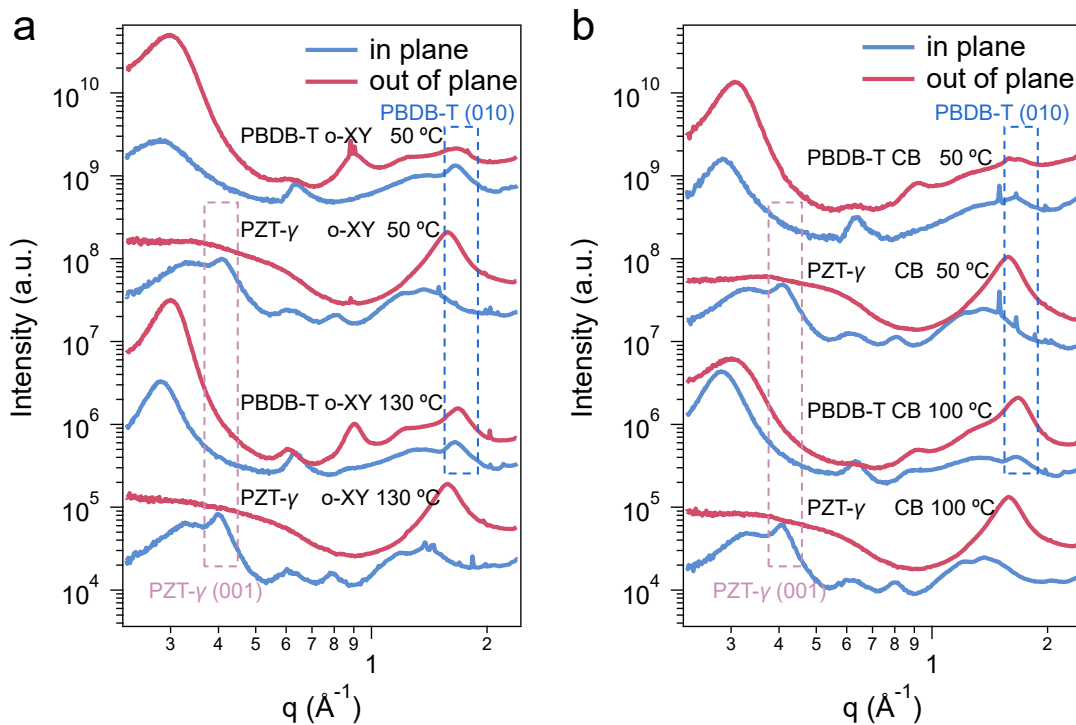


Fig. S9 GIWAXS line profiles of neat PBDB-T and PZT- γ films prepared by o-XY (a) and CB (b) at different temperatures.

Table S3 Structure parameters of the films based on PBDB-T:PZT- γ obtained from GIWAXS.

Processing condition	out of plane							
	Location (\AA^{-1})	FWHM	d-spacing (\AA)	CL (\AA)	Location (\AA^{-1})	FWHM	d-spacing (\AA)	CL (\AA)
o-XY 50 °C	0.302	0.1189	20.79	47.58	1.600	0.3404	3.927	16.61
o-XY 130 °C	0.301	0.0659	20.88	85.86	1.607	0.2856	3.910	19.80
CB 50 °C	0.303	0.1285	20.74	44.01	1.606	0.3323	3.912	17.02
CB 100 °C	0.294	0.0983	21.34	57.53	1.604	0.2973	3.917	19.02

Processing condition	in plane							
	Location (\AA^{-1})	FWHM	d-spacing (\AA)	CL (\AA)	Location (\AA^{-1})	FWHM	d-spacing (\AA)	CL (\AA)
o-XY 50 °C	0.290	0.1340	21.66	42.20	0.411	0.0646	15.28	87.60
o-XY 130 °C	0.290	0.0531	21.70	106.49	0.398	0.0545	15.80	103.84
CB 50 °C	0.290	0.1104	21.64	51.24	0.406	0.0797	15.49	70.96
CB 100 °C	0.290	0.0574	21.69	98.46	0.395	0.0746	15.91	75.81

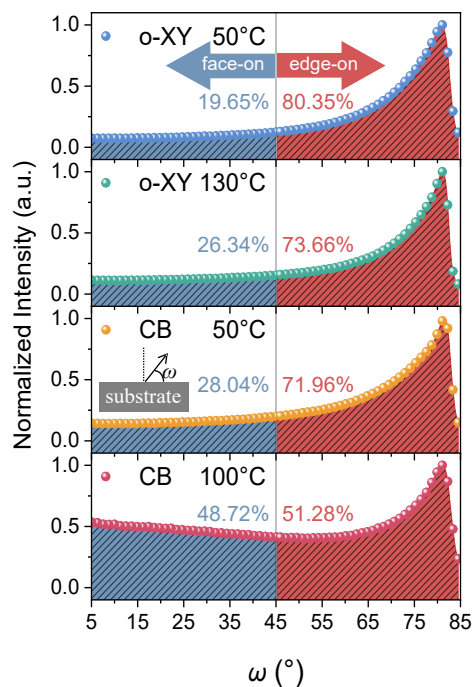


Fig. S10 Pole figure of (100) diffraction peak for neat PBDB-T films.

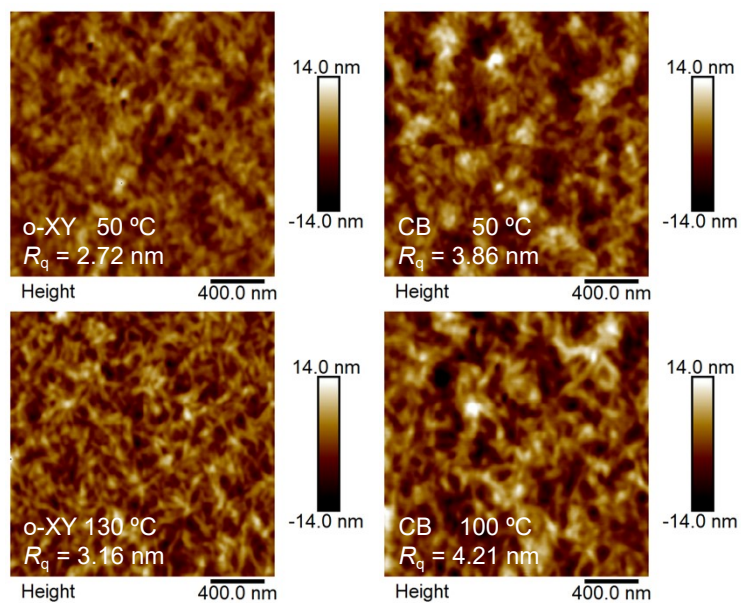


Fig. S11 AFM height images for the o-XY treated PBDB-T:PZT- γ films and CB treated PBDB-T:PZT- γ films.

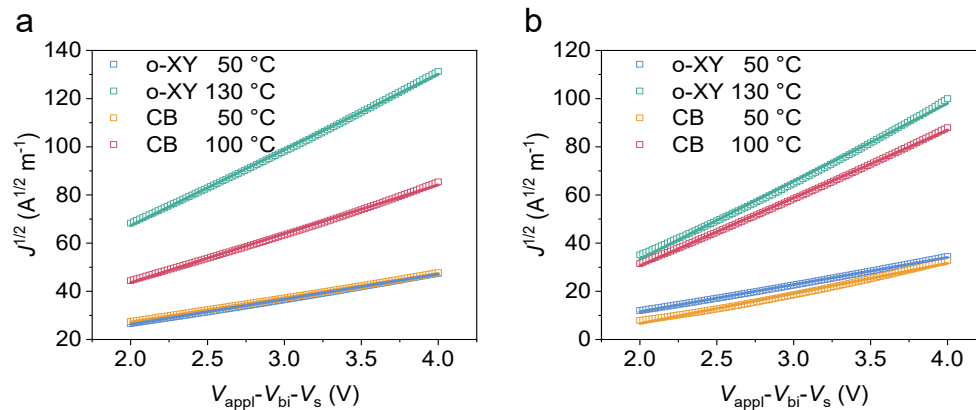


Fig. S12 $J^{1/2}$ - V characteristics of (a) hole-only and (b) electron-only devices for PBDB-T:PZT- γ films with different processing conditions.

Table S4 The summarized hole mobility and electron mobility for PBDB-T:PZT- γ films with different processing conditions.

Processing condition	μ_h [$\times 10^{-4} \text{ cm}^2 \text{ V}^{-1} \text{ s}^{-1}$]	μ_e [$\times 10^{-4} \text{ cm}^2 \text{ V}^{-1} \text{ s}^{-1}$]	μ_e/μ_h
o-XY 50 °C	0.34	0.42	1.2
o-XY 130 °C	3.31	3.50	1.1
CB 50 °C	0.36	0.52	1.4
CB 100 °C	1.38	2.66	1.9

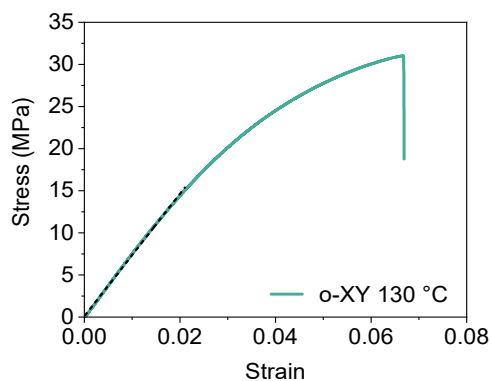


Fig. S13 Strain-stress curves of o-XY 130 °C processed film (black line is a linear fit to the elastic region).

Table S5 Detailed photovoltaic parameters of o-XY 130 °C processed large-area all-PSCs (1.0 cm²) based on PBDB-T:PZT- γ under AM 1.5G 100 mW cm⁻² illumination. (Average PCE obtained from 8 devices).

Processing condition	V_{oc} [V]	J_{sc} [mA/cm ²]	FF [%]	PCE [%]
o-XY 130 °C	0.874	24.54	53.07	11.38 (11.03±0.28)

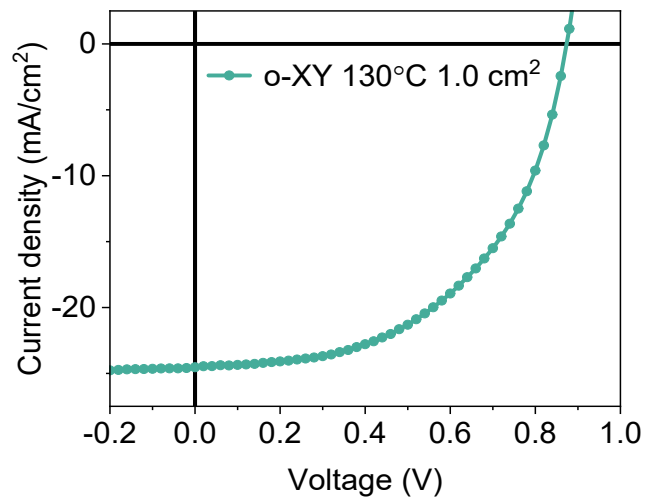


Fig. S14 J - V curve of o-XY 130 °C processed large-area all-PSCs (1.0 cm²) based on PBDB-T:PZT- γ .

References

- [1] H. Fu, Y. Li, J. Yu, Z. Wu, Q. Fan, F. Lin, H. Y. Woo, F. Gao, Z. Zhu, A. K.-Y. Jen, *J. Am. Chem. Soc.*, 2021, **143**, 2665.
- [2] S. Chen, Y. Liu, L. Zhang, P. C. Y. Chow, Z. Wang, G. Zhang, W. Ma, H. Yan, *J. Am. Chem. Soc.*, 2017, **139**, 6298.
- [3] A. Hexemer, W. Bras, J. Glossinger, E. Schaible, E. Gann, R. Kirian, A. MacDowell, M. Church, B. Rude, H. Padmore, *J. Phys. Conf. Ser.*, 2010, **247**, 12007.
- [4] E. Gann, A. T. Young, B. A. Collins, H. Yan, J. Nasiatka, H. A. Padmore, H. Ade, A. Hexemer, C. Wang, *Rev. Sci. Instrum.*, 2012, **83**, 45110.
- [5] Y. Long, S. J. Stuard, H. Ade, *Conjug. Poly. CRC Press*, 2019, 427.
- [6] X. Jiao, L. Ye, H. Ade, *Adv. Energy Mater.*, 2017, **7**, 1700084.
- [7] Y. Xiong, L. Ye, C. Zhang, *J. Polym. Sci.*, 2022, **60**, 945.
- [8] M.-J. Li, B.-B. Fan, W.-K. Zhong, Z.-M.-Y. Zeng, J.-K. Xu, L. Ying, *Chin. J. Polym. Sci.*, 2020, **38**, 791.
- [9] Y. Zhou, K. L. Gu, X. Gu, T. Kurosawa, H. Yan, Y. Guo, G. I. Koleilat, D. Zhao, M. F. Toney, Z. Bao, *Chem. Mater.*, 2016, **28**, 5037.
- [10] H. Jung, A.-R. Jung, S.-M. Jin, S. Kim, H. Heo, H. V. T. Nguyen, M. J. Kim, P. Ahn, M. H. Kim, Y. Lee, K.-K. Lee, J. H. Cho, E. Lee, B. Kim, *Nano Energy*, 2020, **77**, 105106.
- [11] Q. Zhang, Z. Chen, W. Ma, Z. Xie, Y. Han, *J. Mater. Chem. C*, 2019, **7**, 12560.
- [12] S. Li, H. Zhang, W. Zhao, L. Ye, H. Yao, B. Yang, S. Zhang, J. Hou, *Adv. Energy Mater.*, 2016, **6**, 1501991.
- [13] Q. Zhang, Z. Chen, W. Ma, Z. Xie, J. Liu, X. Yu, Y. Han, *ACS Appl. Mater. Interfaces*, 2019, **11**, 32200.
- [14] Z. Li, L. Ying, P. Zhu, W. Zhong, N. Li, F. Liu, F. Huang, Y. Cao, *Energy Environ. Sci.*, 2019, **12**, 157.
- [15] B. Fan, W. Zhong, L. Ying, D. Zhang, M. Li, Y. Lin, R. Xia, F. Liu, H.-L. Yip, N. Li, Y. Ma, C. J. Brabec, F. Huang, Y. Cao, *Nat. Commun.*, 2019, **10**, 4100.
- [16] Y. Meng, J. Wu, X. Guo, W. Su, L. Zhu, J. Fang, Z.-G. Zhang, F. Liu, M. Zhang, T. P. Russell, Y. Li, *Sci. China Chem.*, 2019, **62**, 845.

- [17] Z. Li, W. Zhong, L. Ying, F. Liu, N. Li, F. Huang, Y. Cao, *Nano Energy*, 2019, **64**, 103931.
- [18] T. Gokulnath, J. Choi, H. Jin, H.-Y. Park, K. Sung, Y. Do, H. Park, S. S. Reddy, J. Kim, M. Song, J. Yoon, S.-H. Jin, *ACS Appl. Mater. Interfaces*, 2021, **13**, 28231.
- [19] H. Liu, L. Wang, H. Liu, M. Guan, C.-J. Su, U.-S. Jeng, B. Zhao, C. Weng, K. You, X. Lu, *Chem. Eng. J.*, 2022, **429**, 132407.
- [20] C. Zhu, Z. Li, W. Zhong, F. Peng, Z. Zeng, L. Ying, F. Huang, Y. Cao, *Chem. Commun.*, 2021, **57**, 935.
- [21] H. Yu, S. Luo, R. Sun, I. Angunawela, Z. Qi, Z. Peng, W. Zhou, H. Han, R. Wei, M. Pan, A. M. H. Cheung, D. Zhao, J. Zhang, H. Ade, J. Min, H. Yan, *Adv. Funct. Mater.*, 2021, **31**, 2100791.
- [22] J. Zhang, T. Jia, C.-H. Tan, K. Zhang, M. Ren, S. Dong, Q. Xu, F. Huang, Y. Cao, *Sol. RRL*, 2021, **5**, 2100076.
- [23] L. Jin, R. Ma, H. Liu, W. Xu, Z. Luo, T. Liu, W. Su, Y. Li, R. Lu, X. Lu, H. Yan, B. Z. Tang, T. Yang, *ACS Appl. Mater. Interfaces*, 2021, **13**, 34301.
- [24] B. Liu, H. Sun, J.-W. Lee, J. Yang, J. Wang, Y. Li, B. Li, M. Xu, Q. Liao, W. Zhang, D. Han, L. Niu, H. Meng, B. J. Kim, X. Guo, *Energy Environ. Sci.*, 2021, **14**, 4499.
- [25] K. Hu, C. Zhu, K. Ding, S. Qin, W. Lai, J. Du, J. Zhang, Z. Wei, X. Li, Z. Zhang, L. Meng, H. Ade, Y. Li, *Energy Environ. Sci.*, 2022, **15**, 4157-4166.
- [26] L. Ye, Y. Xiong, H. Yao, A. Gadisa, H. Zhang, S. Li, M. Ghasemi, N. Balar, A. Hunt, B. T. O'Connor, J. Hou, H. Ade, *Chem. Mater.*, 2016, **28**, 7451.
- [27] L. Ye, Y. Xiong, S. Li, M. Ghasemi, N. Balar, J. Turner, A. Gadisa, J. Hou, B. T. O'Connor, H. Ade, *Adv. Funct. Mater.*, 2017, **27**, 1702016.
- [28] B. Lin, L. Zhang, H. Zhao, X. Xu, K. Zhou, S. Zhang, L. Gou, B. Fan, L. Zhang, H. Yan, X. Gu, L. Ying, F. Huang, Y. Cao, W. Ma, *Nano Energy*, 2019, **59**, 277-284.
- [29] L. Zhu, W. Zhong, C. Qiu, B. Lyu, Z. Zhou, M. Zhang, J. Song, J. Xu, J. Wang, J. Ali, W. Feng, Z. Shi, X. Gu, L. Ying, Y. Zhang, F. Liu, *Adv. Mater.*, 2019, **31**, 1902899.